AAS 20-711

COMPRESSED SENSING FOR SATELLITE CHARACTERIZATION

Daigo Kobayashi* **and Carolin Frueh†**

Characterization of space objects around the Earth is an essential step in space situational awareness. However, direct resolved imaging is rarely possible because of the large distances between a sensor and an object. This research discusses a potential application of a compressed sensing technique to characterize an unknown stabilized satellite in a known orbit from its non-resolved light curve. Compressed sensing was originally developed for efficient signal compression and reconstruction. In this paper, simulations showed that compressed sensing is capable of reconstructing resolved satellite images based solely on non-resolved light curves, assuming a reference observation is available to estimate the so-called sensing matrix. This result implies the great potential of compressed sensing in characterizing space objects.

INTRODUCTION

In a framework of space situational awareness (SSA), it is necessary to detect new objects, track the detected objects, and characterize them to predict their locations and identify them. Characterization implies the size, shape, and attitude of unknown space objects. There exist some methods to tackle this problem by using an imaging approach. One of the most acclaimed examples is the FGAN Tracking and Imaging Radar (TIRA),[1] which is capable of obtaining a resolved image of a 10-m size satellite in Low Earth orbit (LEO) by Ku-band radar. However, most Earth-orbiting objects are too small or remote to be imaged with even the most state-of-the-art ground-based instrument.

On the other hand, a light curve-based method can be applied to objects in higher orbits including geosynchronous orbits with an altitude of 35786 km. The basic idea is to estimate the shape or orientation of an object based on its light curve, which is a time history of the intensity of light reflected on an object. This approach has been used to characterize celestial objects. M.Kaasalainen ad J.Torppa[2,3] succeeded in obtaining a three-dimensional shape of asteroids including a moderately nonconvex object. With a steady spinning attitude profile, light curve-based approaches also have been used for artificial satellites. However, the characterization of man-made objects requires additional efforts because of their properties: complex surface properties, unstable attitudes, and highly concave shapes. Calef et al.[4] utilized thermal emissions and a light curve to recover the three-dimensional shape of an object, assuming its orientation to the observer is known and the object is convex. Linares et al.[5] used angles data and light curves to estimate the most probable shape of an object by using the unscented Kalman filter. Linares and Crassidis[6] obtained shape and surface parameters of a space object by the Bayesian inversion approach. Recently, Furfaro et al.[7] used a deep learning method to classify the shape of space objects into four categories. Fan, Friedman,

*Research Assistant, School of Aeronautics and Astronautics Engineering, Purdue University, dkobayas@purdue.edu.
†Associate Professor, School of Aeronautics and Astronautics Engineering, Purdue University, cfrueh@purdue.edu.

and Frueh[8,9,10] implemented the light curve inversion considering the fact that real observations are greatly affected by observation noise and the conditions for obtaining sufficient data for inversion.

Although much improvement has been made for the light curve inversion problem, it is still challenging to estimate attitude, shape, and surface parameters simultaneously. Even when concentrating on the shape inversion problem alone, the problem is an ill-posed problem, which often has multiple solutions and ambiguities. Therefore, this research proposes an imaging method that reconstructs a resolved image of observed space objects based solely on the non-resolved light curve data. The method to be used is based on the so-called compressed sensing.

Compressed sensing (CS) is a novel signal compression theory, which is capable of recovering compressible unknown signals from a small number of random measurements even if they are inaccurate and incomplete. A signal is compressed as a linear measurement by using a so-called sensing matrix and then the signal is reconstructed by solving an optimization problem. The number of measurements required by CS is far fewer than those required by the traditional Shannon/Nyquist sampling theorem,[11] leading to a paradigm shift in the signal processing field. In the field of aerospace engineering, there have been some applications to enjoy this benefit. Aguilera et al.[12,13] used the CS in a synthetic aperture radar (SAR) tomography to improve the quality of reconstructions. Daponte et al.[14] used the CS framework to design radio frequency (RF) sensors for localization and tracking of non-cooperative RF emitters. In remote sensing, CS led to new onboard instruments called MPST and SPMT camera, which needed less storage space and less power consumption than classical CCD cameras[15].[16] It is also possible to apply CS to obtain clear pictures from incomplete measurements.[17] However, there are no examples of CS applications to a light curve measurement so far.

Under some assumptions, a light curve of an object may be regarded as an object image compressed by atmospheric noise, which is considered in this paper as a pseudo-sensing matrix in the CS framework. However, there is a significant difference that hinders the direct application of CS into a light curve. Since the atmospheric noise is a random process, no information is available about the pseudo-sensing matrix, which makes the CS reconstruction a challenging task.

The approach presented in this paper is to utilize a previous or simultaneous observation of a known satellite. This approach is similar to a technique called adaptive optics.[18] In astronomical observations, a star is obscured by unwanted wavefront distortions due to atmospheric turbulence. The adaptive optics technique removes the effect of the distortions by observing a reference star or an artificial laser-generated reference star.[19] This research shows that this idea is also feasible for estimating a sensing matrix.

The organization of this paper is as follows. First, theories of compressed sensing and its relevance of a specific setup using a single-pixel camera are introduced. Second, the simulation scheme of a light curve considering the atmospheric noise and attenuation is developed. That is used to generate the results presented in this paper. The new model for this attenuated noisy light curve is then compared with compressed sensing and a single-pixel camera. Subsequently, theories and algorithms for noise removal techniques are introduced, which are used in the post-processing of this research. Finally, an explicit satellite image is recovered from the attenuated noisy light curve by new approaches based on the assumption that known satellites are observed simultaneously. Two approaches are developed according to the availability of the known satellites.

COMPRESSED SENSING

Theory

Compressed sensing is a mathematical theory proposed by Candes, Romberg, Tao[2021] and Donoho[22] in 2006. It is also sometimes referred to as compressive sampling or compressed sampling. It has been widely used in signal compression methods such as JPEG, JEPG2000, MPEG, and MP3 standards.

In compressed sensing, a signal is sampled directly in a compressed form:

$$\bar{y} = \mathbf{\Phi}\bar{x} \tag{1}$$

where $\bar{x} \in \mathbb{R}^N$ is an image vector, $\bar{y} \in \mathbb{R}^m (m \ll N)$ is a measurement vector, and $\mathbf{\Phi} \in \mathbb{R}^{m \times N}$ is a so-called sensing matrix. The sensing matrix compresses the image signal by mapping a high dimensional vector into a lower-dimensional vector. This enables to sample an image signal in a sampling rate which is much lower than that of the Shannon/Nyquist sampling theorem.[11]

For the success of compressed sensing, a signal needs to be either sparse or compressible. A sparse signal is a vector with only k nonzero elements. In other words, the L_0 norm of $\bar{x}$, or the cardinality of $\bar{x}$ is k:

$$\bar{x} \ \in \mathbb{R}^N \quad \text{with } \|\bar{x}\|_0 = k \ (\ll N) \tag{2}$$

However, most signals themselves are not sparse but can be expressed sparsely in terms of a certain basis. This kind of signal is called a compressible signal, which is mathematically expressed as follows:

$$\bar{x} = \mathbf{\Psi}\bar{\gamma} \ \in \mathbb{R}^N \quad \text{with } \|\bar{\gamma}\|_0 = k \ (\ll N) \tag{3}$$

The matrix $\mathbf{\Psi}$ is typically square and called a sparsifying matrix. In this research, a discrete cosine transform (DCT) matrix[23] is used for this sparsifying matrix since most natural images are known to be compressible by this matrix.

Another key element of compressed sensing is a sensing matrix $\mathbf{\Phi}$. For a stable reconstruction, the sensing matrix needs to satisfy a measure called Restricted Isometry Property (RIP).[24] Candes[25] showed that randomness in the matrix guarantees the RIP. Therefore, this research uses a Gaussian matrix whose entries are i.i.d. Gaussian random variables with zero-mean and $1/N$-variance as a sensing matrix.

If the signal $\bar{x}$ is sparse or compressible, and if the sensing matrix $\mathbf{\Phi}$ satisfies the RIP, the signal $\bar{x}$ is guaranteed to be recovered from the measurement $\bar{y}$ by seeking the sparsest representation of the signal $\bar{x}$:

$$\hat{\gamma} = \text{argmin} \|\bar{\gamma}\|_0 \quad \text{s.t. } \bar{y} = \mathbf{\Phi}\mathbf{\Psi}\bar{\gamma} \tag{4}$$

However, since this problem is sensitive to a perturbation, more robust alternatives are often solved:

$$\hat{\gamma} = \text{argmin } \|\bar{y} - \mathbf{\Phi}\mathbf{\Psi}\bar{\gamma}\|_2^2 \quad \text{s.t. } \|\bar{\gamma}\|_0 = K \tag{5}$$

$$\hat{\gamma} = \text{argmin } \|\bar{\gamma}\|_0 \qquad \text{s.t. } \|\bar{y} - \mathbf{\Phi}\mathbf{\Psi}\bar{\gamma}\|_2^2 \leq \varepsilon^2 \tag{6}$$

Eq.(5) is a sparsity-constraint problem while Eq.(6) is an error-constraint problem. Theoretically, the solutions of these two problems are the same. One of these two problems is chosen according to which information is given.

The most well-known solvers for these optimization problems are greedy methods and relaxation methods. The greedy methods build a solution by choosing one nonzero element at a time, while the relaxation methods approximate the problem as a continuous optimization problem. In this research, one of the greedy methods, the batch orthogonal matching pursuit (batch-OMP) method[26] will be used because of its fast computation time. It lowers the computational cost of the classical OMP method by implementing a progressive Cholesky update, and by pre-computing a Gram matrix and some other coefficients.

Single-Pixel Camera

One of the most important applications of compressed sensing is a single-pixel camera introduced by Takhar et.al.[27] In compressed sensing, a linear measurement of a signal is implemented using a sensing matrix. With a closer look at Eq.(1), each entry of the measurement vector (referred to as y_i) is an inner product between a row of the sensing matrix (referred to as $\bar{\phi}_i^T$) and the signal $\bar{x}$. Suppose the size of the signal is $n^2 \times 1$, these two vectors are reshaped into square matrices $\mathbf{\Phi}$ and $\mathbf{X}$. The entry y_i is expressed as a summation of the element-wise product between these two matrices:

$$y_i = \bar{\phi}_i^T \, \bar{x} = \sum_{\text{all}} \mathbf{\Phi}_i \odot \mathbf{X} \tag{7}$$

where $\odot$ stands for the element-wise product. Therefore, the measurement vector $\bar{y}$ in Eq.(1) can be obtained by getting the element-wise product m times. This idea is practiced in a single-pixel camera.

Figure 1 shows a schematic diagram of the single-pixel camera. This camera measures a scene by first focusing the scene on a digital micromirror device (DMD) array by a convex lens. The DMD is a grid of millions of micromirrors, each of which corresponds to each pixel of the observed scene. The light fluxes are reflected off the mirrors in one of two directions: toward or away from the photodiode, depending on the orientation of each micromirror. Only the light fluxes reflected toward the photodiode are collected by a second lens and measured by a photodiode. One can see that this DMD works as a binary alternative of the sensing matrix. The measurement is repeated m times with different mirror patterns in DMD to get a measurement vector $\bar{y}$, and reconstruction is implemented by CS solver. As a result, this camera is capable of imaging a scene with only one single photodiode.

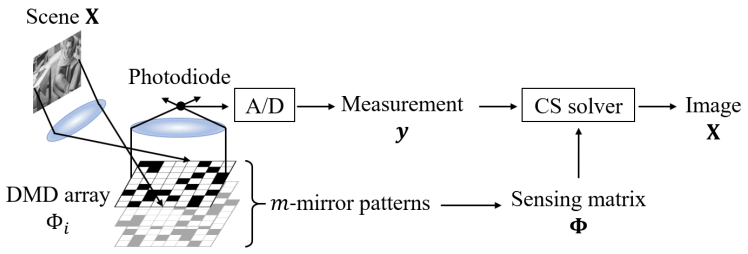

Figure 1. Single-pixel camera diagram

ATTENUATED NOISY LIGHT CURVE MODEL

Light curve simulation

A light curve is defined as a time series of brightness measurements of an observed object.[28] The intensity of the light curve is observed by collecting the light which is reflected off the surface of a space object. It depends on the geometric shape, surface properties, and positional relationship between the object, the Sun, and the observer. In this research, a light curve is simulated by modeling a satellite as a 3D polygon model consisting of triangle facets by using the so-called ray tracing technique. In the ray tracing, visible facets are selected from the polygon model by checking three conditions: 1) the facet has to be above the observer's local horizon, 2) the observer and the Sun must be on the same side of the facet, 3) the facet must not be hidden by other facets.[29] The third condition needs extra care, and two cases need to be considered as shown in Figure 2. The first case, (a), is a self-shadowing in which a light flux coming into a facet is obstructed by another facet. The second case, (b), is an observer-shadowing in which a light flux coming out from a facet is obstructed by another facet. Facets that pass all these three conditions are considered visible.

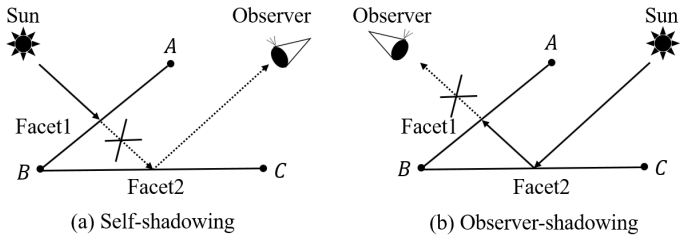

Figure 2. Two Kinds of Shadowing in Ray Tracing

The light intensity of each visible facet is computed by using the bi-directional reflectance distribution function (BRDF) model which consists of the Lambertian reflection term and the specular reflection term:

$$I(t) = I_0 \sum_{i=1}^{n} \frac{A_i}{\pi (r_{\text{topo}})^2} (\bar{S} \cdot \bar{N}_i) \left\{ C_d (\bar{V} \cdot \bar{N}_i) + \frac{\pi \tau_i C_s (r_{\text{Sun}})^2}{a_{\text{Sun}}^2} \right\} \tag{8}$$

where I_0 is the solar irradiance at 1 AU, n is the total number of facets, A_i is the i-th facet area, $\bar{N}_i$ is the i-th facet normal, r_{topo} is the distance between the object and the observer, $\bar{V}$ is the object-to-the-observer vector, $\bar{S}$ is the object-to-the-Sun vector, C_d is the diffuse reflection parameter, and C_s is the specular reflection parameter. The specular reflection is a mirror-like reflection which is concentrated in a particular direction. Because of the finite size of the Sun, it allows half a degree difference between the incoming and the outgoing light flux:

$$\tau_i = \begin{cases} 1 & \text{if } |\theta_{incoming} - \theta_{outgoing}| \leq 0.5^\circ \\ 0 & \text{otherwise} \end{cases} \tag{9}$$

Synthetic Resolved Image Generation

Similarly, a synthetic image of the satellite is also generated by the rendering technique to see how the satellite is illuminated. The basic idea is to set an imaginary image plane consisting of grids,

which are referred to as *pixels*, in front of the observer. Light from the Sun reflects off the surface of the satellite, passes through one of the pixels in the image plane, and reaches to the observer. Each pixel value is determined so that it is approximately the same value with the intensity of the light which comes through the pixel.

The first step of the rendering is the orthogonal projection of the 3D polygon model onto the image plane. The coordinates of all the vertices of the 3D polygon model are transformed into a new coordinate so that the z-axis is parallel to the object-to-the-observer vector, and the new xy-plane is parallel to the image plane. These new (x,y)-positions of the vertices are rounded to the nearest integer and converted to the pixel coordinates. The z coordinates of the vertices are called *depths*, which is significant information in a later procedure.

The next step is rasterization. The vertices of the facets on the image plane are connected by line segments based on the facet information of the original polygon model. The rasterization technique approximates the line segments as a collection of pixels based on the digital differential analyzer (DDA) algorithm.[30] After all the edges are drawn on the image plane, the pixels circumscribed by the edges are filled out by the scanline algorithm[30] to approximate the facets on the image plane.

In the rasterization, pixel values need to be assigned to each pixel by a so-called shading technique. First, the brightness of each facet is computed in the same way as that of the light curve simulation. This facet brightness corresponds to the total pixel value of the facet. In computer graphics, there are some ways to distribute this facet brightness to each pixel. In this research, a method called flat shading is used, where each pixel value is determined by simply dividing the facet brightness by the number of pixels in the facet.

Another important procedure in the rasterization is hidden surface removal. Since all the facets are projected onto the image plane in the first step, some facets which are hidden by other facets are also displayed in the image. In such a case, multiple facets are overlapped on the image but only one of them needs to be shown. This correction is done by the z-buffer algorithm using the z coordinates, or depths, of the vertices obtained in the first step. This algorithm chooses the facet closest to the observer and computes the pixel value based on the facet.

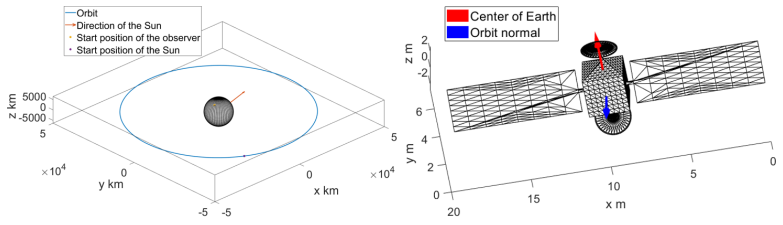

(a) Geosynchronous orbit based on TLE data of Astra 1KR satellite

(b) 3D model of Astra 1KR satellite

Figure 3. Orbit and 3D Satellite Model Used in the Simulation

The combination of all these techniques generates an image of the satellite model. One example simulation is implemented as follows. The Astra 1KR satellite is modeled as a 3D model shown in Figure 3 (b), which consists of 4028 facets. The surface property of these facets is set to be: $C_d = 0.8$, $C_s = 0.2$ assuming that the satellite is made of aluminum, which is one of the most common materials for spacecraft. The reflection property highly depends on the finish but its diffuse reflection coefficient is often assumed to be around 0.8-0.9.[29] The orbit is computed based on

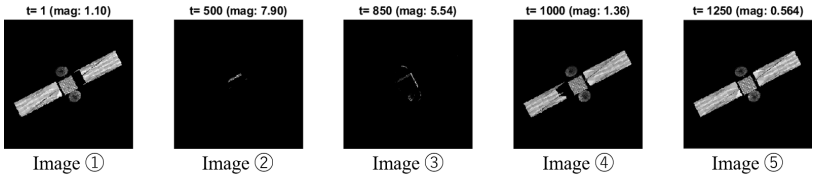

(a) Synthetic Images of Satellite

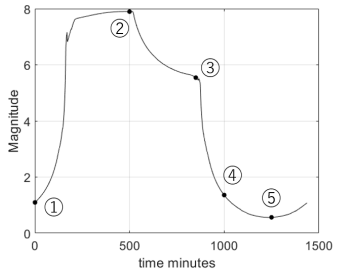

(b) Simulated Light Curve

Figure 4. Atmosphere-free Light Curve and Corresponding Synthetic Satellite Images

the TLE data of Astra 1KR satellite obtained from the Space-track organization website.[31] It is propagated for 1437 minutes by SGP4 propagator from the initial epoch, 0:00:00 AM on 1-April-2020 UTC. The resultant orbit is a geosynchronous orbit with nearly zero eccentricity. The observer is located in Berlin at 51.17^o N, 10.45^o E.

The orientation of the satellite also needs to be defined. Active satellites are traditionally either spin-stabilized or three-axis stabilized. Here, a three-axis stabilized satellite is assumed. Since the parabolic antennas always need to be oriented toward the Earth, one facet of the satellite body (red arrow in Figure 3 (b)) is fixed to the direction of the geocenter, and another facet (blue arrow in Figure 3 (b)) is fixed so that it is always perpendicular to its orbital plane. Therefore, the solar panels are not always oriented toward the Sun in this simplified simulation.

Figure 4 shows the results of a simulated light curve and corresponding synthetic satellite images. The five images correspond to the five points of the simulated light curve. The summation of the pixel values in each image is approximately equal to the light curve intensity at that time step. With a closer look at the images, it is obvious that the magnitude of the light curve increases and get fainter as the satellite has more shade.

Attenuated noisy light curve model

It is important to note that the light curve in Figure 4 does not consider attenuation or corruption by atmospheric noise. In this case, all the light fluxes from the satellite reach to the observer without being disturbed and hence the light curve intensity is a sum of the light intensity of all the facets:

$$I(t) = \bar{1}^T \bar{\rho}(t) = \sum_{i=1}^{n} \rho_i \tag{10}$$

where ρ_i denotes a light intensity of the i-th facet. In a real light curve observation, on the other hand, light fluxes from a space object pass through a turbulent atmosphere around the Earth before they reach a ground-based sensor. Due to the fluctuation of refraction index of the atmosphere,

the irradiance of light fluxes is affected unevenly. Some light fluxes may not be affected much while other fluxes may be weakened severely or reflected toward the observer. Therefore, the most straightforward way to model the noisy light curve is to simply exchange the vector $\bar{1}$ in Eq.(10) for a Gaussian random vector, $\bar{\xi}$:

$$I(t) = \bar{\xi}^T \bar{\rho}(t) = \sum_{i=1}^{n} \xi_i \rho_i \tag{11}$$

where ρ_i is the light intensity of the i-th facet. This model is referred to as the *attenuated noisy LC model*.

However, this model is not straightforward in terms of the application to compressed sensing. As an approximation, this research uses an adapted model using a pixel-wise noise instead of a facet-wise noise. First, a synthetic satellite image is generated corresponding to a light curve. This image is vectorized and multiplied by a Gaussian random vector, $\bar{\phi}$:

$$I(t) = \bar{\phi}^T \bar{x}(t) = \sum_{i=1}^{n_{\text{pixel}}} \phi_i x_i \tag{12}$$

where n_{pixel} is a total number of pixels in the synthetic satellite image, and x_i is the i-th pixel value of the image. This model is referred to as the *simplified attenuated noisy LC model*.

Figure 5 shows a comparison of the effect of the different light curve models. The black line graph is the same one in Figure 4. Compared to this atmosphere-free light curve, the attenuated noisy light curves are shifted to higher magnitudes and are thus fainter, as expected. The simplified attenuated noisy LC model results in a larger shift, whereas the overall noisy structure seems to be mostly preserved.

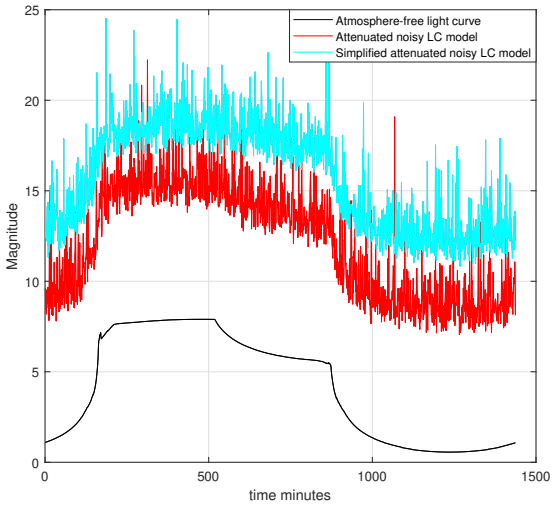

Figure 5. Comparison Between Atmosphere-free Light Curve and Attenuated Noisy Light Curves

Comparison with Compressed Sensing

The example above considers an observation of a geostationary satellite over 24 hours for illustration purposes. On the other hand, for realistic shorter light curve observations over limited time frames, the solar motion is minimal, and the geostationary satellite looks approximately constant during m measurements especially when its attitude is stabilized:

$$\bar{x}_i = \bar{x} = \text{constant}, \ \forall\, i = 1, \ldots, m \tag{13}$$

However, conditions of the atmospheric turbulence change even for the instantaneous period. Thus, each satellite image should be subject to different atmospheric noise. Therefore, m intensity values of the light curve are expressed by using the simplified attenuated noisy LC model as follows:

$$y_1 = \bar{\phi}_1 \bar{x}, \ \ldots \ , y_m = \bar{\phi}_m \bar{x} \tag{14}$$

The set of equations in (14) can be concatenated and expressed in the form of a matrix equation:

$$\bar{y} = \mathbf{\Phi} \bar{x} \tag{15}$$

This expression is exactly the same as that of a compressed signal (1) in compressed sensing where the atmospheric noise matrix $\mathbf{\Phi}$ corresponds to a sensing matrix. Therefore, hereinafter, the simplified attenuated noisy LC model is used for simulating the attenuated noisy light curve.

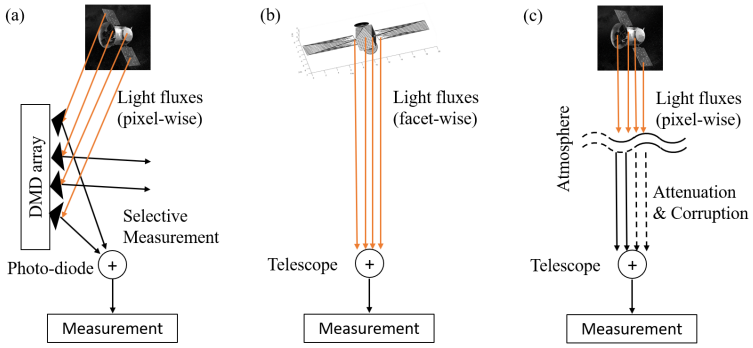

Figure 6. Comparison of a Single-pixel Camera and a Light Curve: (a) Observation by a Single-pixel Camera, (b) Observation via Atmosphere-free Light Curve, (c) Observation via Simplified Attenuated Noisy Light Curve

This analogy can also be explained by a comparison between a single-pixel camera and a light curve as shown in Figure 6. First, in an observation by a single-pixel camera, the light irradiance from an object is multiplied by a random ratio based on the mirror pattern of a DMD array, and their total intensity is measured by a photodiode as shown in Figure 6 (a). Similarly, in a light curve observation, light fluxes reflected off a satellite are collected by a sensor. If the light fluxes are not disturbed by the atmosphere, the light curve is a simple sum of the irradiance of the light fluxes as shown in Figure 6 (b). However, in reality, light fluxes are attenuated and corrupted by atmospheric turbulence. Therefore, the irradiance of the light fluxes is scaled randomly before being observed. Thus, the attenuated noisy light curve measurement can be regarded as one measurement in a single-pixel camera, and hence it has similarity with compressed sensing.

However, in a real observation, it is almost impossible to know the atmospheric noise beforehand and hence the matrix $\mathbf{\Phi}$ is unavailable in Eq.(15). Therefore, the main goal of this research is to reconstruct a satellite image $\bar{x}$ based on its attenuated noisy light curve $\bar{y}$ without prior knowledge of the sensing matrix $\mathbf{\Phi}$.

DENOISING ALGORITHMS

In this research, noisy images are cleaned by the denoising algorithm as post-processing. In the framework of compressed sensing, an image without noise is modeled using a matrix $\mathbf{D}'$ and a sparse coefficient vector $\bar{\gamma}$:

$$\bar{x} = \mathbf{D}'\bar{\gamma} \quad \text{with } \|\bar{\gamma}\|_0 \leq T \tag{16}$$

This matrix $\mathbf{D}'$ is often referred to as a *dictionary*. A noisy image, on the other hand, is modeled by adding noise $\bar{v}$ to this clean image:

$$\bar{z} = \mathbf{D}'\bar{\gamma} + \bar{v} \quad \text{with } \|\bar{v}\|_2 \leq \varepsilon' \tag{17}$$

where the noise $\bar{v}$ is often modeled as a Gaussian noise upper-bounded by ε. A basic idea to remove noise from the noisy image $\bar{z}$ is to find the best pair $\{\hat{\gamma}, \hat{D}'\}$ whose representation error is within ε'. However, the direct estimation of these variables is usually a challenging task.

One way to circumvent this issue is a so-called dictionary learning technique using training data obtained by a patch-based method. First, overlapped patches of size $p \times p$ are extracted from a noisy image. They are vectorized and concatenated to form a training data matrix, $\mathbf{Z}$ as shown in Figure 7. It is assumed that the sparse representation described by Eq.(17) also exists locally for these small patches:

$$\mathbf{Z} = \mathbf{D}\mathbf{\Gamma} + \mathbf{E} \quad \text{with } \|\mathbf{E}\|_F \leq \varepsilon \tag{18}$$

Based on this model, the denoising problem can be formulated as:

$$\{\hat{\mathbf{\Gamma}}, \hat{\mathbf{D}}\} := \text{argmin } \|\bar{\gamma}_i\|_0 \quad \text{subject to } \|\mathbf{Z} - \mathbf{D}\mathbf{\Gamma}\|_F \leq \varepsilon \tag{19}$$

where $\bar{\gamma}_i$ is the i-th column of the matrix $\mathbf{\Gamma}$.

There are several methods to solve this denoising problem. In this research, sparse-KSVD (k-singular value decomposition) algorithm[32] is chosen because of its fast computation and high accuracy. In this algorithm, the problem is simplified by a model called the *double sparsity model*. It is assumed that the dictionary $\mathbf{D}$ also has a sparse representation in terms of a base dictionary, $\mathbf{D}_0$:

$$\mathbf{D} = \mathbf{D}_0\mathbf{A} \quad \forall i,\ \|\bar{a}_i\|_0 \leq T_0 \tag{20}$$

where $\bar{a}_i$ is the i-th column of the matrix $\mathbf{A}$. This assumption decreases the number of variables and shortens the computation time. In this research, a DCT matrix is chosen for the base dictionary $\mathbf{D}_0$. Using this double sparsity model, Eq.(19) is restated as follows:

$$\{\hat{\mathbf{\Gamma}}, \hat{\mathbf{A}}\} := \text{argmin } \|\bar{\gamma}_i\|_0 \quad \text{subject to } \|\mathbf{Y} - \mathbf{D}_0\mathbf{A}\mathbf{\Gamma}\|_F \leq \varepsilon,\ \forall i,\ \|\bar{a}_i\|_0 \leq T_0 \tag{21}$$

The sparse-KSVD algorithm solves this problem by updating $\mathbf{\Gamma}$ and $\mathbf{A}$ alternately. While one of them is fixed, the other is updated. This cycle is repeated until the stopping criterion is satisfied.

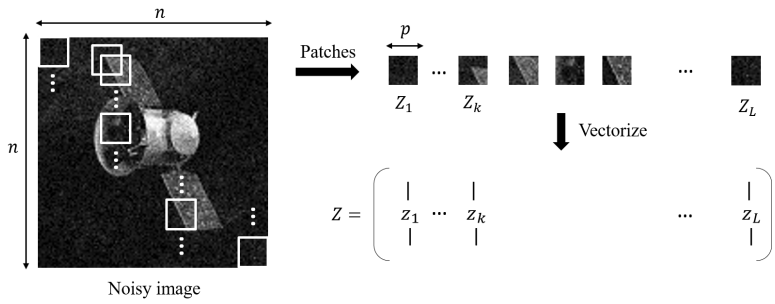

Figure 7. Procedure for Obtaining Training Data by Patch-based Method

In this paper, the sparse-KSVD algorithm is used in two different ways. In the first method, the algorithm is used to remove noise from one single noisy image as introduced above. This approach is referred to as a 2D sparse-KSVD algorithm because it is applied to a two-dimensional image. In the second method, on the other hand, the algorithm is expanded to a three-dimensional image, which is called 3D sparse-KSVD algorithm. When multiple noisy images from a common source are available, they are piled to form a 3D image. From this 3D noisy image, 3D cubes instead of 2D patches are extracted to form training data by patch-based method, and a 3D dictionary is learned by solving Eq.(21). This 3D sparse-KSVD algorithm performs better than the 2D sparse-KSVD algorithm because it uses knowledge of a structure shared by multiple images.

REFERENCE SATELLITE APPROACH

This research proposes a method to estimate a target satellite image by compressed sensing without prior knowledge of the sensing matrix $\mathbf{\Phi}$. This method assumes that some known satellites (hereinafter referred to as *reference satellites*) are simultaneously observed with a target satellite under common atmospheric conditions. In this paper, it is assumed that the resolved images of the reference satellite are available in conjunction with the measured light curve of the reference satellite.

This method is similar to an idea called a guide star in adaptive optics. The adaptive optics system is a technique to improve the resolution of the astronomical images by sensing and correcting the atmospheric aberrations.[18] In this technique, a reference star or a guide star is observed to estimate the atmospheric turbulence effect. This knowledge enables to adjust a deformable primary mirror to get much sharper images of other stars than images obtained without adaptive optics. The guide star can be either a heavenly body or an artificial star such as a sodium laser.[19]

Inspired by the idea of a guide star, it is assumed that there are N reference satellite images of size $n \times n$ are available. These images are vectorized and concatenated to form a matrix $\mathbf{X}_{\text{ref}} \in \mathbb{R}^{n_{\text{pixel}} \times N}$ where $n_{\text{pixel}} = n^2$. Using this matrix, the light curves of the reference satellite images are expressed as:

$$\mathbf{Y}_{\text{ref}} = \mathbf{\Phi}\mathbf{X}_{\text{ref}} \tag{22}$$

Note that the sensing matrix $\mathbf{\Phi}$ in Eq.(22) is the same as the one in Eq.(15) since the target satellite and reference satellites are observed under the common atmospheric conditions. This research proposes an idea to use Eq.(22) to estimate the sensing matrix $\mathbf{\Phi}$. There are two different approaches according to the value of N, the number of reference satellites available.

Full Rank Matrix Approach

The first approach assumes that an abundant number of reference satellite images are available:

$$N = n_{\text{pixel}} \tag{23}$$

Moreover, these images are varied enough to be linearly independent, which is nearly always true if the images are corrupted by random noise. Under these assumptions, the matrix $\mathbf{X}_{\text{ref}}$ in Eq.(22) becomes a full rank matrix. Therefore, the sensing matrix $\mathbf{\Phi}$ can be simply obtained by inverting the matrix $\mathbf{X}_{\text{ref}}$:

$$\hat{\mathbf{\Phi}} = \mathbf{Y}_{\text{ref}}\mathbf{X}_{\text{ref}}^{-1} \tag{24}$$

After the sensing matrix $\mathbf{\Phi}$ is estimated, the target satellite image can be estimated by solving Eq.(15) by CS solver.

Rank-deficient Matrix Approach

The second approach considers a much realistic case where the number of images and light curves of reference satellites are not sufficient for a full rank condition:

$$N < n_{\text{pixel}} \tag{25}$$

In this case, the matrix $\mathbf{X}_{\text{ref}}$ is a horizontal matrix, and hence Eq.(22) has infinitely many solutions.

However, with a closer look at the matrix $\mathbf{X}_{\text{ref}}$, one can notice that it is a sparse matrix because the background of most satellite images is black. Moreover, it also has randomness due to corruption by white noise. Therefore, the matrix $\mathbf{X}_{\text{ref}}$ roughly satisfies the RIP condition, and it can be considered as a sensing matrix. Thus, the matrix $\mathbf{\Phi}$ is modeled as a compressible signal:

$$\mathbf{\Phi}^T = \mathbf{\Psi}\mathbf{A} \quad \text{s.t. } \forall i, \|\bar{a}_i\|_0 \leq T_0 \tag{26}$$

where a vector $\bar{a}_i$ is the i^{th} column of the coefficient matrix $\mathbf{A}$, and $\mathbf{\Psi}$ is a DCT matrix. Using this expression, Eq.(22) is reduced to the following form:

$$\mathbf{Y}_{\text{ref}}^T = \mathbf{X}_{\text{ref}}^T\mathbf{\Psi}\mathbf{A} = \mathbf{D}\mathbf{A} \quad \text{s.t. } \forall i, \|\bar{a}_i\|_0 \leq T_0 \tag{27}$$

where $\mathbf{D} = \mathbf{X}_{\text{ref}}^T\mathbf{\Psi}$. The matrix $\mathbf{A}$ can be obtained by solving either of the following problems by CS solver in a column-wise way:

$$\hat{a}_i = \text{argmin } \|\bar{y}_i - \mathbf{D}\bar{a}_i\|_2^2 \quad \text{s.t. } \|\bar{a}_i\|_0 = T_0 \tag{28}$$

$$\hat{a}_i = \text{argmin } \|\bar{a}_i\|_0 \qquad \text{s.t. } \|\bar{y}_i - \mathbf{D}\bar{a}_i\|_2^2 \leq \varepsilon_0^2 \tag{29}$$

where $\hat{y}_i$ represents the i^{th} column of the matrix $\mathbf{Y}_{\text{ref}}^T$. Once the matrix $\mathbf{A}$ is estimated, the sensing matrix can be computed as:

$$\hat{\mathbf{\Phi}} = \hat{\mathbf{A}}^T\mathbf{\Psi}^T \tag{30}$$

Using this estimated sensing matrix, Eq.(15) can be solved by CS solver.

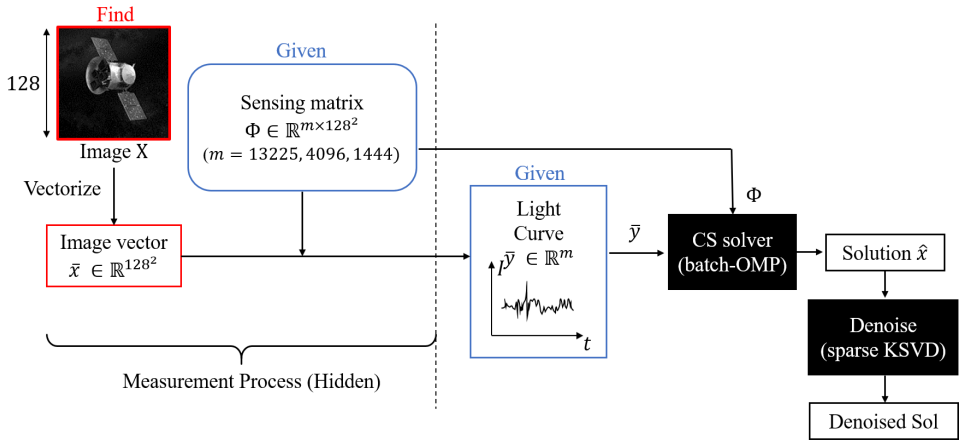

Figure 8. Flowchart of Simulation 1

CHARACTERIZATION OF A SATELLITE BY COMPRESSED SENSING

In the following, the characterization of a satellite by compressed sensing is simulated under three different scenarios. The first scenario is a proof-of-concept simulation where the sensing matrix $\mathbf{\Phi}$ is assumed to be known. The second scenario tests the validity of the full rank matrix approach. It considers a case where the sensing matrix $\mathbf{\Phi}$ is unavailable but many images and light curves of the reference satellites are available. Finally, the third scenario tests the validity of the rank-deficient matrix approach. It considers the worst case where the sensing matrix $\mathbf{\Phi}$ is unavailable, and images and light curves of the reference satellites are also limited.

In all these scenarios, it is assumed that the target satellite is stabilized and located in a known geostationary orbit, and the reference satellites are located in the proximity. The observer is located at an arbitrary ground station.

Simulation 1: Proof-of-concept Simulation

The procedure for this simulation is shown in Figure 8. A target satellite image is NASA's TESS satellite[33] of size 128×128. A vector $\bar{x}$ represents a vectorized target image and it is measured by three different sensing matrices to get light curves in Eq.(15). These sensing matrices are all generated by Gaussian random variables with mean 0 and variance $1/n_{\text{pixel}}$ where $n_{\text{pixel}} = 128^2$ but with different number of measurements, $m = 13325,\ 4096,\ 1444$. Finally, the target image is reconstructed by solving Eq.(5) or Eq.(6) by the batch-OMP algorithm. The noise of the solution is removed by 2D sparse-KSVD algorithm.[32] This simulation aims to show that the target satellite image can be reconstructed by a compressed sensing scheme in the presence of the sensing matrix. Therefore, in this particular simulation, the sensing matrices are given, and reference satellites are not observed. Moreover, the impact of the number of measurements on the reconstruction is investigated by comparing the results from three different sensing matrices.

The results are shown in Figure 9. The images in the first column show the simplified attenuated noisy light curves, $\bar{y}$ obtained in this simulation. The images in the second column show the reconstructed results, and the ones in the third column show the denoised results. For the case of the largest number of measurements $m = 13325$, the reconstructed image clearly shows the shape

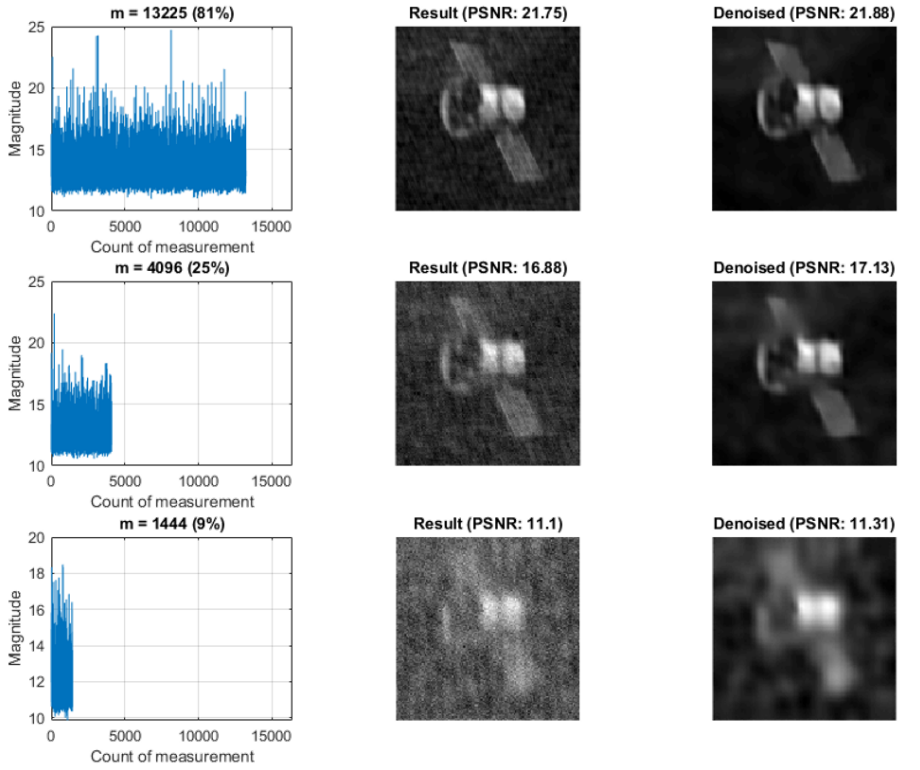

(a) Light Curves (b) Recovered Images (c) Denoised Images

Figure 9. Results of Simulation 1

of the target satellite, and it becomes even clearer after being denoised. For the case of a reduced number of measurements $m = 4096$, the reconstructed image deteriorates but the denoised image clearly shows the satellite shape. For the case of the smallest number of measurements $m = 1444$, the reconstructed image hardly shows the satellite shape but it becomes clear enough to identify the satellite shape after being denoised.

Simulation 2: Full Rank Matrix Approach

In this simulation, the full rank matrix approach is illustrated. The procedure for this simulation is shown in Figure 10. A target satellite image is the same as simulation 1. A vector $\bar{x}$ represents a vectorized target satellite image and it is measured by a sensing matrix $\mathbf{\Phi}$ to get a light curve $\bar{y}$.

Subsequently, reference satellite images of size 128×128 are generated based on a 3D satellite model. The satellite is assumed to be in a geostationary orbit and it is illuminated and observed from random directions. The total number of images is 128^2. They are corrupted by white noise, vectorized, and concatenated to form a full rank matrix $\mathbf{X}_{\text{ref}}$. These images are measured by a sensing matrix $\mathbf{\Phi}$ to get a set of light curves $\mathbf{Y}_{\text{ref}}$.

Assuming the matrices $\mathbf{X}_{\text{ref}}$ and $\mathbf{Y}_{\text{ref}}$ are known, the sensing matrix $\mathbf{\Phi}$ is estimated using Eq.(24). Using this estimated matrix $\hat{\mathbf{\Psi}}$ and the light curve $\bar{y}$, the target satellite image is reconstructed by solving Eq.(5) or Eq.(6) by the batch-OMP algorithm.

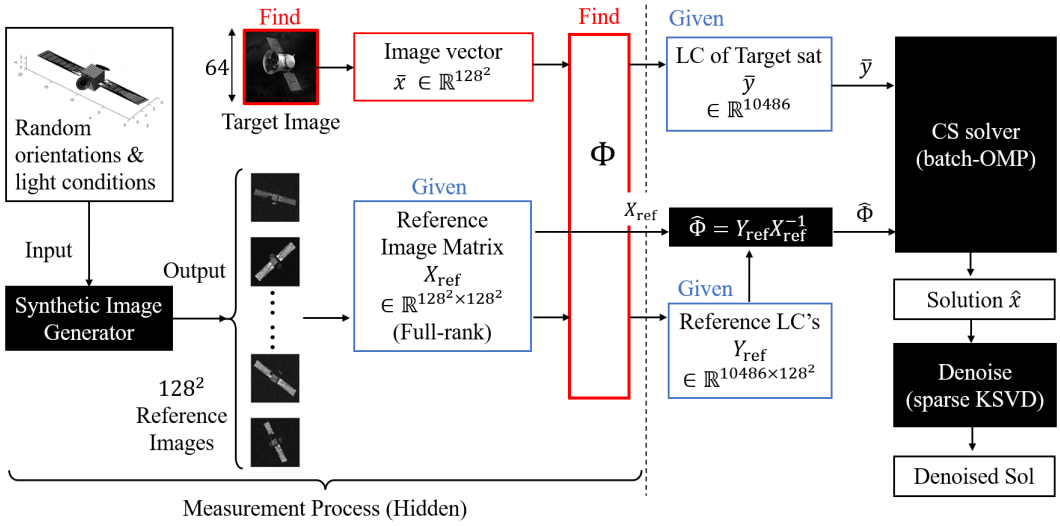

Figure 10. Flowchart of Simulation 2

The results are shown in Figure 11. It took about 68 minutes to finish the computation in the Space Information Dynamics (SID) group server. The first image is the true image for the sake of comparison. The second image is a reconstructed result directly obtained by this approach. Although this approach perfectly estimates the sensing matrix, the reconstructed result is noisy. This is because of an error in the reconstruction process due to the nature of a Gaussian matrix. In general, the use of a Gaussian matrix as a sensing matrix tends to cause some errors in compressed sensing, and hence it is necessary to apply some noise removal methods as a post-process. The third image is the result denoised by the 2D sparse-KSVD algorithm. The PSNR value has increased by 3.87 dB and the image is almost identical with the true image. Although some parts of the solar panels and the star sensor baffle are still not clear, this result is clear enough to identify the satellite.

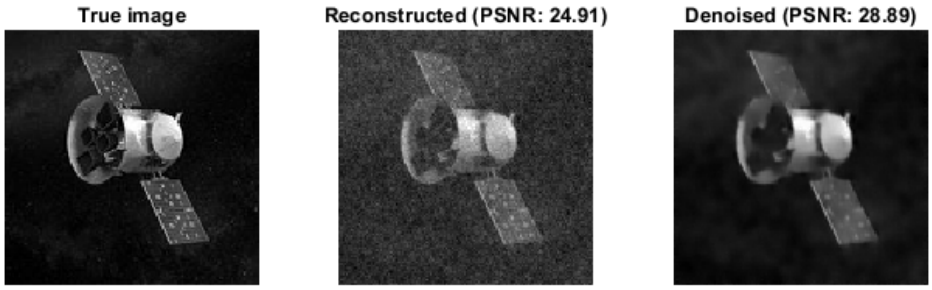

Figure 11. Results of Simulation 2

Simulation 3: Rank-deficient Matrix Approach

In this simulation, the rank-deficient matrix approach is illustrated. The procedure for this simulation is shown in Figure 12. A target satellite image is the same with simulation 1 but it is smaller

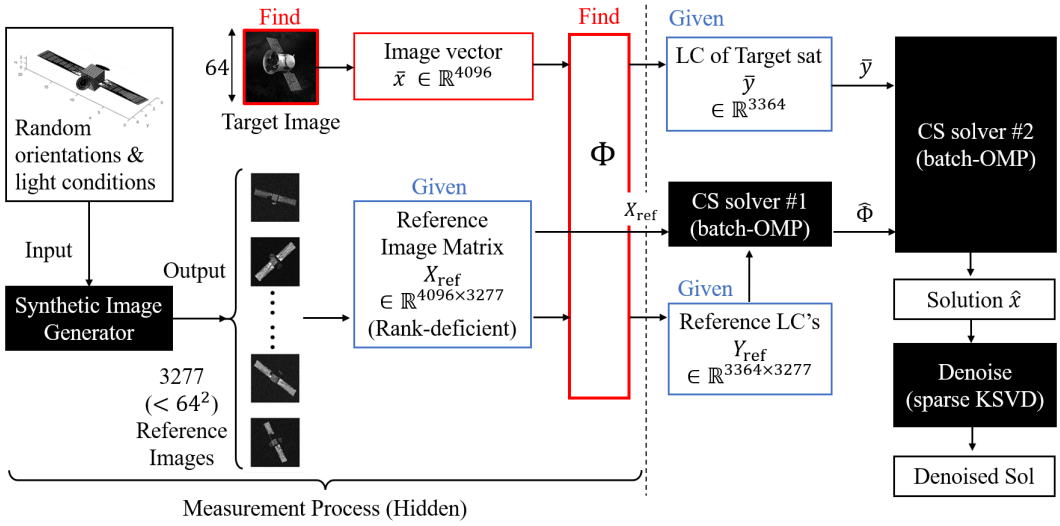

Figure 12. Flowchart of Simulation 3

(64×64) to avoid too much computational cost in the estimation of $\mathbf{\Phi}$. A vector $\bar{x}$ represents a vectorized target satellite image and it is measured by a sensing matrix $\mathbf{\Phi}$ to get a light curve $\bar{y}$.

Second, reference satellite images of size 64×64 are generated based on a 3D satellite model. The satellite is assumed to be in a geostationary orbit and it is illuminated and observed from random directions. The total number of images is 8000. Among these images, 3277 images are randomly chosen to form a matrix $\mathbf{X}_{\text{ref}}$ because the choice of the reference satellite images greatly affects the result of this simulation. These images are measured by a sensing matrix $\mathbf{\Phi}$ to get a set of light curves $\mathbf{Y}_{\text{ref}}$.

Assuming the matrices $\mathbf{X}_{\text{ref}}$ and $\mathbf{Y}_{\text{ref}}$ are known, the sensing matrix $\mathbf{\Phi}$ is estimated by solving Eq.(28) or Eq.(29) by the batch-OMP algorithm. Using this estimated matrix $\hat{\mathbf{\Psi}}$ and the light curve $\bar{y}$, the target satellite image is reconstructed by solving Eq.(5) or Eq.(6) by the batch-OMP algorithm. The noise of the solution is removed by 2D sparse-KSVD algorithm.

This whole process is repeated 9 times with a different set of reference satellite images. These 9 different results are merged to form a 3D-image of size $64 \times 64 \times 9$ and its noise is removed by 3D sparse-KSVD algorithm. One purpose of this operation is to see the impact of the choice of the reference satellite images. This approach considers the matrix $\mathbf{X}_{\text{ref}}$ as a sensing matrix. Thus, the result highly depends on the choice of the reference images. Another purpose of this operation is to improve the quality of the noise removal. Since the matrix $\mathbf{X}_{\text{ref}}$ does not perfectly follow the RIP condition, the quality of the result would be worse than simulation 1. To compensate this defect, the noise is removed by the 3D sparse-KSVD, which considers a common structure between the 9 results and gives better performance.

Figure 13 shows 9 results directly obtained by this approach. Even though the same procedures are repeated 9 times, their PSNR values differ from each other. This is because a different set of reference satellite images has been used for these results. The chosen reference satellite images have been used to form a reference image matrix $\mathbf{X}_{\text{ref}}$. This matrix is then used as a sensing matrix to estimate the matrix $\mathbf{\Phi}$. The quality of the estimated $\mathbf{\Phi}$ affects the solution of the target image. As

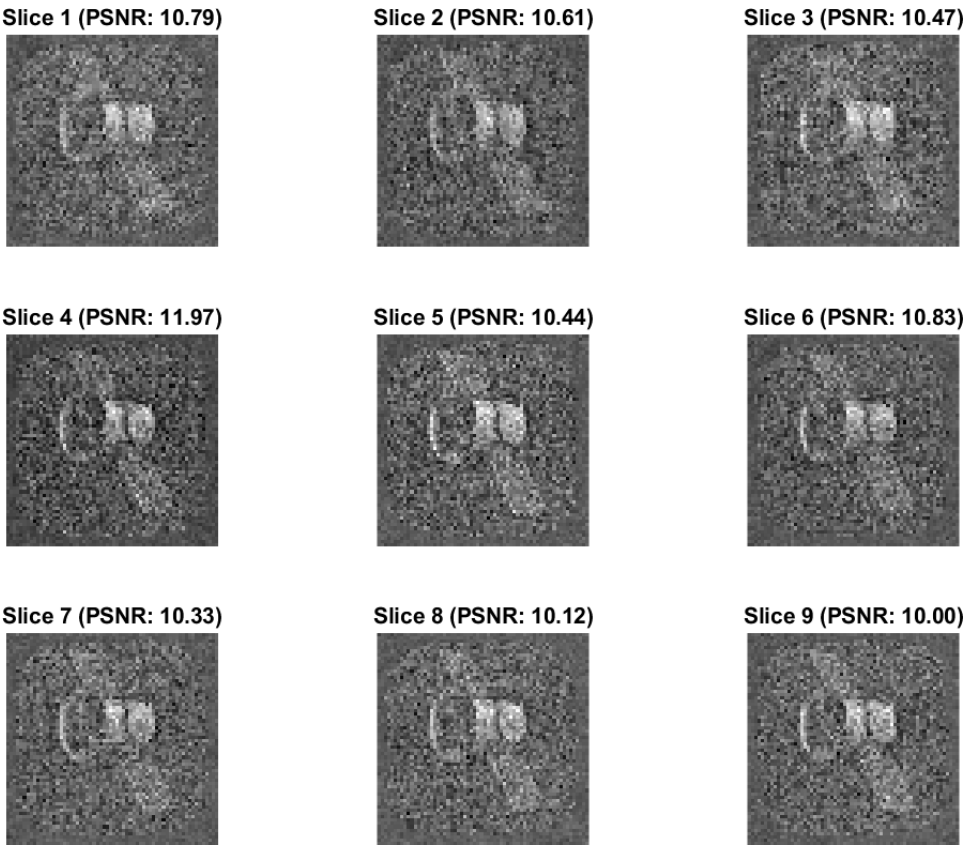

Figure 13. Noisy Results of Simulation 3

a result, the choice of reference satellite images has affected the quality of the target image. This also explains why these 9 results are much noisier than the result in Figure 11. In this simulation, the estimation of the matrix $\mathbf{\Phi}$ is never better than that of simulation 2 because of the ill-designed sensing matrix $\mathbf{X}_{\text{ref}}$. It does not strictly follow the RIP condition which is required to guarantee a stable reconstruction in compressed sensing. For the same reason, the computation time gets longer, and it took about 8 hours to finish the procedure per image in the SID group server.

Figure 14 compares the true image, one of the noisy results, and two images obtained after denoising. The second image is the slice 4 in Figure 13, which has the largest PSNR value in the noisy results. The third image shows a result obtained by denoising the second image by 2D sparse-KSVD algorithm. The PSNR value has improved by 0.38 dB but it is still noisy. On the other hand, the fourth image shows a result obtained by denoising the 9 slices of images by 3D sparse-KSVD algorithm. The PSNR value has improved by 2.65 dB from the 2D-denoised result, and this result is clear enough to identify the target satellite.

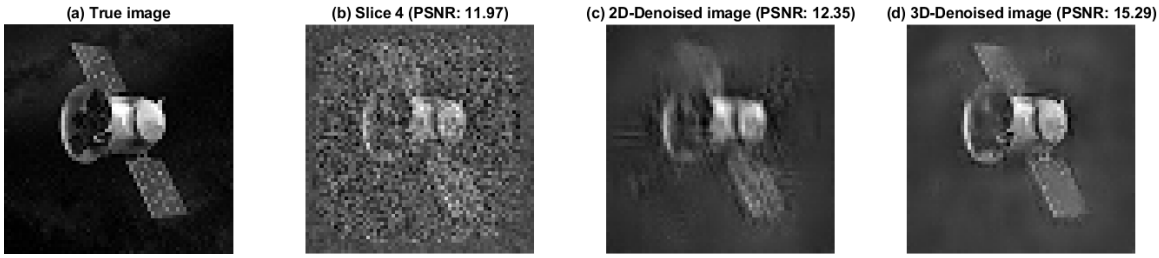

Figure 14. Results of Simulation 3: (a) True Image for Comparison, (b) Best result directly obtained by simulation 3 before denoising, (c) Best result after being denoised by 2D-sparse KSVD algorithm, (d) Best result after being denoised by 3D-sparse KSVD algorithm

CONCLUSIONS

This research has discussed a potential application of a compressed sensing technique to characterize an unknown stabilized satellite in a known orbit from its non-resolved light curve. Compressed sensing is a mathematical theory for efficient signal compression and reconstruction. It enables to reconstruct an image from only a fraction of its linear measurement. This measurement is done by an inner product with a random matrix, which is referred to as a sensing matrix. In this research, it has been compared with light curve measurements, and an adapted light curve model has been introduced by considering attenuation and noise due to atmospheric turbulence. In this model, the atmospheric turbulence is considered as a pseudo-sensing matrix, and the light curve is considered as an image compressed by an unknown sensing matrix. However, the atmospheric turbulence, or the sensing matrix is usually unknown and hence there is a significant deviation from a classical compressed sensing scheme, where the sensing matrix is known.

This research has proposed two approaches to reconstruct an image of a target satellite without the knowledge of the sensing matrix. It has been assumed that the sensing matrix can be inferred from simultaneous observations of a known satellite. In the first case under those assumptions, it is assumed that the images of the reference satellite are abundant enough to construct a full-rank matrix of size $128^2 \times 128^2$. In this case, the sensing matrix and the target image can be estimated accurately. In a more realistic case, only fewer images of the reference satellite would be available. As a result, the reference satellite images are sparse and not sufficient for constructing a full-rank matrix. However, utilizing the sparsity property, the target satellite image estimation is achieved. This has been done by using the batch-OMP algorithm and the three-dimensional sparse KSVD algorithm.

Future work is focused on overcoming the significant limitation of a simultaneous reference satellite observation.

ACKNOWLEDGMENT

The authors thank Prof. Dr. Puneet Singla, Pennsylvania State University for the suggestion to explore compressed sensing in combination with light curve characterization measurements, and hope for future collaboration.

REFERENCES

[1] D. Mehrholz, L. Leushacke, W. Flury, R. Jehn, H. Klinkrad, and M. Landgraf, "Detecting, tracking and imaging space debris," *ESA Bulletin(0376-4265)*, No. 109, 2002, pp. 128–134.

[2] M. Kaasalainen and J. Torppa, "Optimization methods for asteroid lightcurve inversion: I. shape determination," *Icarus*, Vol. 153, No. 1, 2001, pp. 24–36.

[3] M. Kaasalainen, J. Torppa, and K. Muinonen, "Optimization methods for asteroid lightcurve inversion: II. The complete inverse problem," *Icarus*, Vol. 153, No. 1, 2001, pp. 37–51.

[4] B. Calef, J. Africano, B. Birge, D. Hall, and P. Kervin, "Photometric signature inversion," *Unconventional Imaging II*, Vol. 6307, International Society for Optics and Photonics, 2006, p. 63070E.

[5] R. Linares, M. K. Jah, J. L. Crassidis, and C. K. Nebelecky, "Space object shape characterization and tracking using light curve and angles data," *Journal of Guidance, Control, and Dynamics*, Vol. 37, No. 1, 2014, pp. 13–25.

[6] R. Linares and J. L. Crassidis, "Resident Space Object Shape Inversion via Adaptive Hamiltonian Markov Chain Monte Carlo," *AAS/AIAA Space Flight Mechanics Meeting*, 2016, pp. 2016–514.

[7] R. Furfaro, R. Linares, and V. Reddy, "Shape Identification of Space Objects via Light Curve Inversion using Deep Learning Models," *AMOS Technologies Conference, Maui Economic Development Board, Kihei, Maui, HI*, 2019.

[8] S. Fan, A. Friedman, and C. Frueh, "Satellite Shape Recovery from Light Curves with Noise," *amos*, 2019, p. 23.

[9] S. Fan and C. Frueh, "A Direct Light Curve Inversion Scheme in the Presence of Measurement Noise," *The Journal of the Astronautical Sciences*, 2019, pp. 1–22.

[10] A. Friedman, S. Fan, C. Frueh, and T. Schildknecht, "Observability of light curve shape inversion based on optical data," *First International Orbital Debris Conference*, 2019.

[11] H. Nyquist, "Certain topics in telegraph transmission theory," *Transactions of the American Institute of Electrical Engineers*, Vol. 47, No. 2, 1928, pp. 617–644.

[12] E. Aguilera, M. Nannini, and A. Reigber, "Multisignal compressed sensing for polarimetric SAR tomography," *IEEE Geoscience and Remote Sensing Letters*, Vol. 9, No. 5, 2012, pp. 871–875.

[13] E. Aguilera, M. Nannini, and A. Reigber, "Wavelet-based compressed sensing for SAR tomography of forested areas," *IEEE transactions on geoscience and remote sensing*, Vol. 51, No. 12, 2013, pp. 5283–5295.

[14] P. Daponte, L. De Vito, F. Picariello, S. Rapuano, and I. Tudosa, "Compressed sensing technologies and challenges for aerospace and defense RF source localization," *2018 5th IEEE International Workshop on Metrology for AeroSpace (MetroAeroSpace)*, IEEE, 2018, pp. 634–639.

[15] J. Ma, "Single-pixel remote sensing," *IEEE Geoscience and Remote Sensing Letters*, Vol. 6, No. 2, 2009, pp. 199–203.

[16] J. Ma and M. Y. Hussaini, "Extensions of compressed imaging: flying sensor, coded mask, and fast decoding," *IEEE Transactions on Instrumentation and Measurement*, Vol. 60, No. 9, 2011, pp. 3128–3139.

[17] J. Ma and F.-X. Le Dimet, "Deblurring from highly incomplete measurements for remote sensing," *IEEE Transactions on Geoscience and Remote Sensing*, Vol. 47, No. 3, 2009, pp. 792–802.

[18] H. W. Babcock, "Adaptive optics revisited," *Science*, Vol. 249, No. 4966, 1990, pp. 253–257.

[19] C. E. Max, S. S. Olivier, H. W. Friedman, J. An, K. Avicola, B. V. Beeman, H. D. Bissinger, J. M. Brase, G. V. Erbert, D. T. Gavel, *et al.*, "Image improvement from a sodium-layer laser guide star adaptive optics system," *Science*, Vol. 277, No. 5332, 1997, pp. 1649–1652.

[20] E. J. Candès *et al.*, "Compressive sampling," *Proceedings of the international congress of mathematicians*, Vol. 3, Madrid, Spain, 2006, pp. 1433–1452.

[21] E. J. Candes, J. K. Romberg, and T. Tao, "Stable signal recovery from incomplete and inaccurate measurements," *Communications on Pure and Applied Mathematics: A Journal Issued by the Courant Institute of Mathematical Sciences*, Vol. 59, No. 8, 2006, pp. 1207–1223.

[22] D. L. Donoho, "Compressed sensing," *IEEE Transactions on information theory*, Vol. 52, No. 4, 2006, pp. 1289–1306.

[23] A. K. Jain, *Fundamentals of digital image processing*. Englewood Cliffs, NJ: Prentice Hall,, 1989.

[24] M. Elad, *Sparse and redundant representations: from theory to applications in signal and image processing*. Springer Science & Business Media, 2010.

[25] E. J. Candès, J. Romberg, and T. Tao, "Robust uncertainty principles: Exact signal reconstruction from highly incomplete frequency information," *IEEE Transactions on information theory*, Vol. 52, No. 2, 2006, pp. 489–509.

[26] R. Rubinstein, M. Zibulevsky, and M. Elad, "Efficient implementation of the K-SVD algorithm using batch orthogonal matching pursuit," tech. rep., Computer Science Department, Technion, 2008.

[27] D. Takhar, J. N. Laska, M. B. Wakin, M. F. Duarte, D. Baron, S. Sarvotham, K. F. Kelly, and R. G. Baraniuk, "A new compressive imaging camera architecture using optical-domain compression," *Computational Imaging IV*, Vol. 6065, International Society for Optics and Photonics, 2006, p. 606509.

[28] B. D. Warner *et al.*, *A practical guide to lightcurve photometry and analysis*, Vol. 300. Springer, 2006.

[29] S. Fan, C. Frueh, and A. Buzzoni, "A light curve simulation of the Apollo Lunar Ascent module," *AIAA/AAS Astrodynamics Specialist Conference*, No. 5504, 2016.

[30] E. Angel, D. Shreiner, *et al.*, *Interactive computer graphics: a top-down approach with shader-based OpenGL*. Boston: Addison-Wesley,, 2009.

[31] S. Track.org. https://www.space-track.org/auth/login.

[32] R. Rubinstein, M. Zibulevsky, and M. Elad, "Double sparsity: Learning sparse dictionaries for sparse signal approximation," *IEEE Transactions on signal processing*, Vol. 58, No. 3, 2009, pp. 1553–1564.

[33] NASA, "NASA's TESS Discovers its First Earth-size Planet," https://www.nasa.gov/feature/goddard/2019/nasa-s-tess-discovers-its-first-earth-size-planet.